Received: Added at production | Revised: Added at production | Accepted: Added at production
DOI: xxx/xxxx

RESEARCH ARTICLE

Numerical simulation of deformable particles in a Coulter counter

Pierre Taraconat[1,2] | Jean-Philippe Gineys[1] | Damien Isebe[1] | Franck Nicoud[2] | Simon Mendez*[2]

[1]HORIBA Medical, Parc Euromedecine, Rue du Caducee, BP 7290, 34184 Montpellier Cedex 4, France
[2]Institut Montpellierain Alexander Grothendieck, CNRS, Univ. Montpellier, 2 Place Eugene Bataillon, 34095 Montpellier Cedex 5, France

Correspondence
*Simon Mendez, Institut Montpellierain Alexander Grothendieck. Email: simon.mendez@umontpellier.fr

Abstract

In Coulter counters, cells counting and volumetry is achieved by monitoring their electrical print when they flow through a sensing zone. However, the volume measurement may be impaired by the cell dynamics, which may be difficult to control. In this paper, numerical simulations of the dynamics and electrical signature of red blood cells in a Coulter counter are presented, accounting for the deformability of the cells. In particular, a specific numerical pipeline is developed to overcome the challenge of the multi-scale nature of the problem. It consists in segmenting the whole computation of the cell dynamics and electrical response in a series of dedicated computations, with a saving of one order of magnitude in computational time. This numerical pipeline is used with rigid spheres and deformable red blood cells in an industrial Coulter counter geometry, and compared with experimental measurements. The simulations not only reproduce electrical signatures typical of the those measured experimentally, but also allow an analysis of the electrical signature in terms of heterogeneity of the electrical field and dynamics of the particles in the measurement zone. This study provides a methodology for computing the sizing of rigid or deformable particles by Coulter counter, opening the way to a better understanding of cells signatures in such devices.

KEYWORDS:
Computational fluid dynamics; Fluid structure interaction; Immersed Boundary Method; Coulter counter; Impedance measurement; Red blood cells

1 | INTRODUCTION

Particle counting and sizing represents a real interest for diseases diagnosis. Indeed, the number and the volume distribution of Red Blood Cells (RBCs), white blood cells and platelet may change in case of pathology. Hematological parameters may represent useful pathological markers for clinical decision-making: the RBCs volume distribution varies in case of abnormal cells subpopulation [1]. RBCs volume Distribution Width (RDW) and the Mean Cell Volume (MCV) allow a classification of anemia [2], and Yeşil et al. suggest that RDW statistically increases in case of Inflammatory Bowel disease [3], for instance.

In 1953, Coulter [4] introduced a quick and automatic device dedicated to the numeration of a large number of microscopic cells and to the measurement of their volume. The principle is depicted in Fig. 1: particles suspended in an electrolytic solution are pumped into a micro-orifice commonly called sapphire or ruby. An electrical field is imposed with a constant intensity using two electrodes. According to Ohm's law, a particle flowing through the sapphire changes the total resistivity of the system and induces a tension pulse. One particle produces one pulse, and its maximum is generally taken as a measurement of the particle

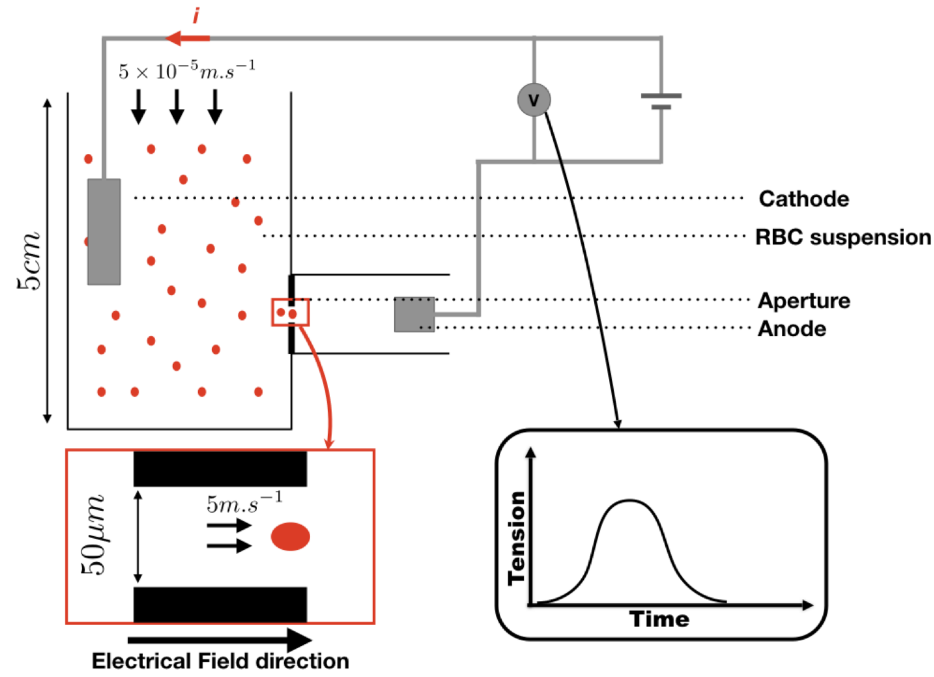

FIGURE 1 Principle of a Coulter counter device for particle counting and sizing.

volume. Thus, counting the pulses and measuring their amplitude give the cell concentration and a volume distribution of those cells.

Analytical studies of Grover et al.[5] and Hurley[6] show that the change of resistivity caused by the presence of an infinitely small and insulating particle in a homogeneous electrical field is proportional to its volume:

$$\Delta R = \frac{\rho_e f_s}{S^2} V, \tag{1}$$

with ΔR the resistance variation, V the particle volume, ρ_e the fluid resistivity, S the aperture cross section and f_s the particle shape factor depending on the shape and orientation of the cell. For example, RBCs are able to deform and reorient when submitted to hydrodynamic forces, which may cause changes in the shape factor. Note that the electrical field in the sensing zone is not homogeneous owing to the device geometry, as shown in numerical simulations of Isèbe & Nérin[7] and the experimental measurements of Kachel[8], contrary to the assumption made in[5,6].

Concerning the electrical field inhomogeneity, the experimental observations of Kachel[8] support a linear relation between the squared electrical field and the electrical perturbation, thus leading to a second version of Eq. 1:

$$\Delta R = \frac{E^2 f_s}{\rho_e i^2} V, \tag{2}$$

The intensity is denoted by i (see Fig. 1) while E designates the electrical field. As the electrical field varies from small values far from the orifice to high values in the sensing zone, the electrical pulse measured during the passage of the particle varies over time, as sketched in Fig. 1.

The volume can thus be determined for specific if and only if the shape factor is known. Analytical developments for the shape factor are available for the case of particles with simple shapes, such as spheres and ellipsoids[5,9] flowing in a homogenous electrical field. The model by Velick et al.[9] may be applied for any ellipsoid with one of its principal axes aligned with the electrical field. Breitmeyer et al.[10] later modeled the impact of the orientation on the shape factor. Qin et al. retrieved numerically the impact of the particle orientation on the electrical resistance variation. Golibersuch obtained pulses presenting several peaks analysing aspherical particles by the use of a Coulter counter with a long aperture[11]. Those peaks are explained by a rotation of the particle that induces a periodic variation of the shape factor.

In summary, the impact of the electrical field inhomogeneity is better understood since Kachel's publication [8] and the shape factor for simple rigid particles is well characterized. However, an understanding of how deformable particles behave in this kind of configuration and influences the shape factor evolution is still lacking.

Due to the difficulties in accessing the RBC dynamics within the measurement zone (small sensing region (tens of μm), large velocity (≈ 5 m.s^{-1}), no optical access, very short time of exposure (10 μs)), numerical simulations would be an appealing way of studying this question. In addition, simulation allows the control of the input parameters, which is always problematic in experiments with biological cells. Numerical simulation of the dynamics and deformation of RBCs under flow has tremendously developed over the last years [12,13,14,15] and its application to Coulter counters is expected to yield new insights in the behavior and the electrical signature of RBCs in the sensing region.

A computation of the entire device is not possible, due to the large number of cells and above all the huge differences in length and time scales when the entire device is considered. As shown in Fig. 1, the size of the measurement region (where the electrical field is high enough so that the cell can be detected) is of a few tens of micrometers and cells pass through the sapphire in a few tens of microseconds. On the contrary, far from the sapphire, they are suspended in a tank of a few centimers (5 cm) and they flow at velocity of the order of 1.0×10^{-3} m.s^{-1}. The separation of scales leads to prohibitive computational times, while the measurement region is actually very limited. An option is to focus on the measurement region only, but cells are known to deform before being detected by the counter [8]. This explains why existing numerical simulations have only considered rigid particles [16,7], thus circumventing the challenge of the scale separation by reducing the computational domain to the region where the impedance signal is detected. This cannot be done when deformable particles are considered.

In this paper, we focus on the simulation of red blood cells, which are the most deformable blood cells. We show that a specific numerical pipeline is needed to accurately compute the impedance signal of a red blood cell passing through a Coulter counter. In particular, a method is provided to compute the state of the red blood cells (orientation and shape) when they enter the measurement zone. Section 2 describes the methodology to compute the impedance pulse associated with the passage of a red blood cell through an industrial Coulter counter. The framework is detailed and the numerical methods are presented. Section 3 shows how the pipeline can be used to decrease the overall computational time (compared with the brute force strategy where the whole Coulter counter is computed) and specifies the conditions under which a relevant simulation can be performed. Finally, section 4 presents numerical results of the computation of rigid and deformable particles in an industrial geometry and compares the results with both theoretical predictions and experimental data. The accuracy of the method is illustrated and simulations are shown to provide useful information about the shape factor in the presence of deformation and rotation of cells.

2 | FROM THE INDUSTRIAL DESIGN TO THE SIMULATION OF THE IMPEDANCE PULSE IN A COULTER COUNTER

2.1 | Overview of the numerical challenge

This section focuses on the principal issues associated with the simulation of an impedance pulse generated by a deformable particle in a Coulter counter, and provides an overview of the method proposed to achieve this task.

Figures 2 A and B show the entirety and a slice cut of the fluid domain that corresponds to an industrial hematology automaton from HORIBA Medical (ABX Micros 60), more precisely the part dedicated to the counting and sizing of the red blood cells in a blood sample. The information presented in the following are based on the operating regime of the Micros 60. The diluted blood sample enters by the boundary indicated as inlet and is vacuumed through the outlet surface (Fig. 2A), while the electrical field is imposed by the electrodes highlighted in Fig. 2B. Examples of electrical and velocity fields obtained by numerical simulation in this industrial configuration are shown in Fig. 2C and 2D. Inside the micro-orifice, the electrical field is very large due to the flux conservation law; this is where particles are detected. The aperture allows to concentrate the electrical field so that the resistance perturbation associated with the passage of a particle is large. In addition, the field decreases rapidly when getting out of the aperture, so that a microscopic particle is not detected outside of the orifice, which allows the sizing of cells one by one if the sample is sufficiently diluted. Due to the contraction of the geometry, the velocity inside the aperture is large, which yields high-throughput measurements, but also generates high velocity gradients and viscous stresses. In particular, high shear stresses are retrieved near the aperture walls. Due to those shear stresses, deformable particles such as RBCs may undergo rotational motions and complex deformations [17]. Before entering in the orifice, the velocity magnitude raises over a short distance, causing large longitudinal strain, so that RBCs elongate to a prolate ellipsoid shape, as reported by Kachel [8] and Gibaud [18]. Far from the aperture, velocity gradients are negligible, and no deformation is expected.

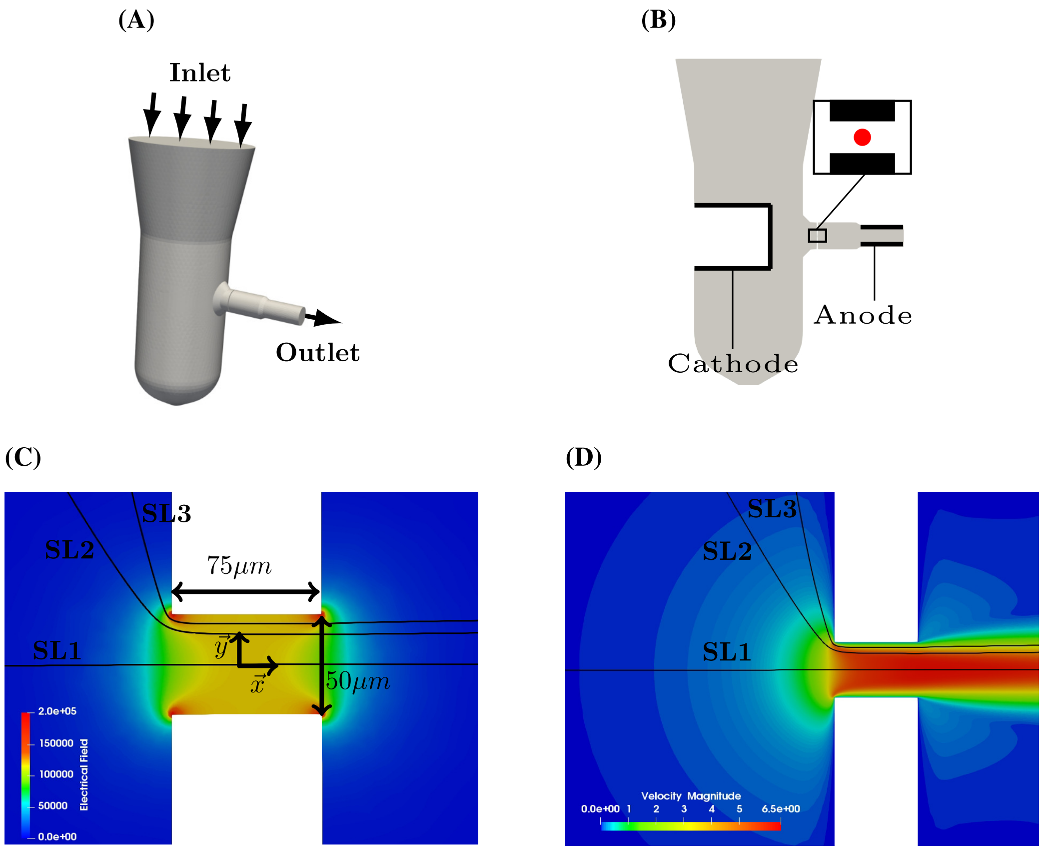

FIGURE 2 A: Fluid domain for red blood cells counting and sizing of ABX Micros 60 (HORIBA Medical). B: Slice cut of the same geometry. The electrodes used for applying the electrical field in the micro-orifice are highlighted. Typical electrical field (C) and velocity field (D) around the aperture. Three different streamlines are depicted in C and D, illustrating the various electrical and velocity field that particles may be subjected to in Coulter counters.

The industrial geometry may be conceptually divided in three parts, as depicted in Fig. 3. Indeed, the RBCs are first transported without deformation in the biggest part of the geometry (Part A). Then, they are stretched just before the aperture entrance by an extensional flow field (Part B). Finally, RBCs are deformed in the micro-orifice while disturbing the electrical field (Part C). Figure 3 B reports the characteristic RBCs transit time in those three parts in the ABX Micros 60 (HORIBA Medical). In the method presented in the following, the choice was made to neglect Part A because no deformation nor electrical perturbation is expected. Thus, only Parts B and C are considered for the modeling. However, as shown in Fig. 3 B, the second part involves a time scale that is larger than the third one by several orders of magnitude. Therefore, instead of simulating the particle evolution in the whole domain where deformations occur (Parts B and C), we propose to split the calculation into two simulations. First, a simulation of the stretching of the cell by a relevant extensional flow is considered. This simulation is referred to as S1. It mimics the elongation happening in Part B of the geometry. A variable strain rate that mimics that seen by the cell is imposed. It is extracted from a first simulation S0, performed on the entire geometry without particles. The calculation in the extensional flow configuration S1 yields a deformed particle, that is used in a second simulation (S2) of the particle dynamics inside the measurement region (Part C). The particle stretched after S1 is placed near of the orifice entrance in a reduced configuration of the whole geometry that is a restricted region around the aperture, in order to reduce the computational cost of S2. Finally, the electrical perturbation is computed by performing a series of electrostatic simulations (S3) using a number of particles position extracted from S2.

The whole procedure is sketched in Fig. 4. In the following sections, each simulation is detailed. First, the setup used to obtain the carrying flow (S0) is presented. Then, the particle stretching process (S1) is detailed. Thereafter, the procedure employed to

(A)

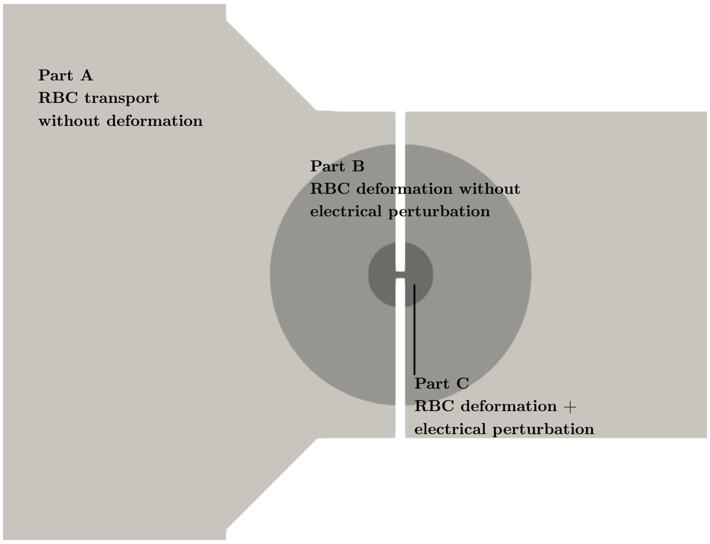

(B)

Part	Time Scale
A	$50s$
B	$12ms$
C	$20\mu s$

FIGURE 3 A: Schematic of the industrial geometry, divided in three parts depending on the existence of particles deformation and the impact on the electrical field. In Part A, the RBC is simply transported without deformations. In Part B, the particle may undergo deformations but is far from the detection area. In Part C, the RBC is deformed and disturbs the electrical field. B: Table presenting characteristic time scales for those three parts, for the case of an ABX Micros 60 (HORIBA Medical).

S0 : Carrying flow ► **S1** : Particle elongation in an axisymmetrical extensional flow ► **S2** : Particle dynamics inside the aperture ► **S3** : Computation of the electrical perturbation

FIGURE 4 Pipeline for the simulation of the electrical perturbation generated by a deformable particle in a Coulter counter.

compute the particle dynamics inside the micro-orifice is explained (S2). Finally, the electrostatic simulations (S3) performed to predict the electrical perturbation are described.

In the following, the case of RBCs is handled as an example of application. However, the pipeline displayed in Fig. 4 may be applied to any deformable particle.

2.2 | Simulation without RBC in the entire fluid domain (S0)

The starting point of the numerical pipeline of Fig. 4 is the simulation of the flow in the whole industrial configuration. The counting tank geometry presented in Fig. 2 includes the aperture where the counting and sizing of RBCs takes place. As already mentionned, it is very small compared to the whole geometry: 50 μm in diameter and 75 μm long. The origin of the coordinates system ($\vec{x}$,$\vec{y}$,$\vec{z}$) is located at the center of the micro-orifice. The aperture is aligned with axis $\vec{x}$ while $\vec{y}$ is included in the middle slice plane shown in Fig. 2B, 2C and 2D; $\vec{z}$ is perpendicular to the ($\vec{x}$,$\vec{y}$) plane.

The electrolytes generally used in Coulter counters are mostly water and typical Reynolds numbers evaluated in industrial systems are higher than 100 (based on bulk velocity in the aperture and diameter). Hence, the flow can be predicted using the Navier-Stokes equations for an incompressible fluid with kinematic viscosity $\nu = 10^{-6}$ m^2.s^{-1} and density $\rho = 1000$ kg.m^{-3} :

$$\frac{\partial \vec{u}}{\partial t} + \vec{u} \cdot \nabla \vec{u} = -\frac{\nabla p}{\rho} + \nabla \cdot [\nu(\nabla \vec{u} + (\nabla \vec{u})^T)] + \vec{f} \tag{3}$$

$$\nabla \cdot \vec{u} = 0 \tag{4}$$

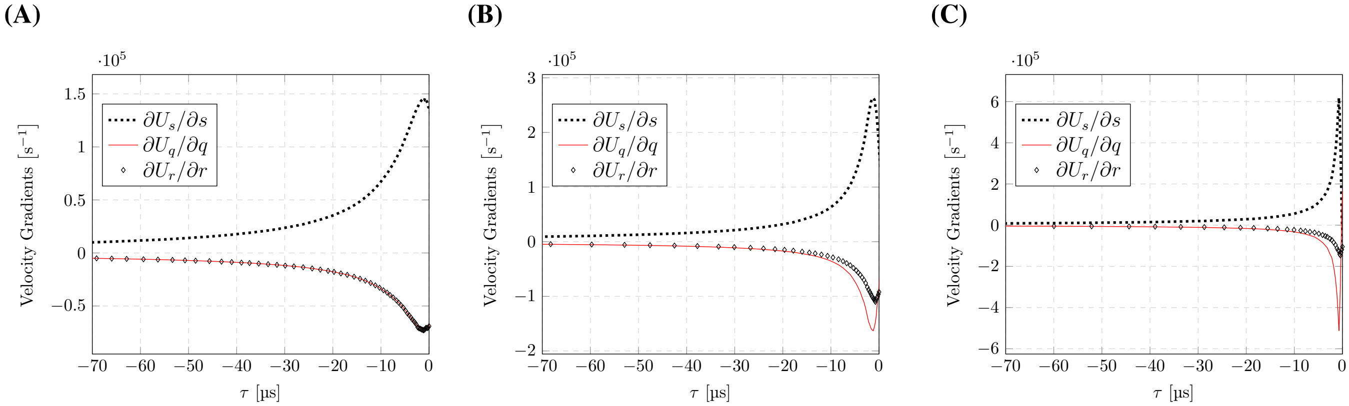

FIGURE 5 Time evolution of the velocity gradients observed by a particle moving along the three different streamlines depicted in Fig. 2, as predicted from the simulation performed on the entire industrial configuration. The graphs A, B and C correspond to the streamlines passing by points (0,0,0), (0,15μm,0) and (0,20μm,0), and are denoted by SL1, SL2 and SL3 in Fig. 2, respectively.

where $\vec{u}$ denotes the fluid velocity, p the pressure, and $\vec{f}$ a possible source term in the momentum equation (in the simulation of the flow in the entire domain, $\vec{f} = \vec{0}$)

The Navier-Stokes equations are solved until the flow convergence inside the aperture is reached. The computation is performed imposing a 7.74×10^{-9} $m^3.s^{-1}$ flow rate at the inlet, which corresponds to a pressure drop of 200 mbar between the upstream and the downstream parts of the micro-orifice. After 50 μs, a stationary flow inside the aperture is obtained. Close enough to the aperture, the flow field is axisymmetric , of axis $\vec{x}$. In the following, the choice of restricting the study to the symmetrical plane ($\vec{x}$,$\vec{y}$) was made.

The flow field is computed using an in-house solver named YALES2BIO (http://imag.umontpellier.fr/~yales2bio), dedicated to the computation of blood flows at the macroscopic [19,20,21] and microscopic scales [17,22,23,24,25,26]. The momentum equation 3 is discretized with a fourth-order finite volume method and advanced in time with a fourth-order Runge-Kutta scheme [27]. The divergence-free condition imposed by mass conservation is achieved by a projection-correction algorithm [28] that involves the resolution of a Poisson equation. This Poisson equation is solved by means of a Deflated Preconditioned Conjugate Gradient algorithm [29].

2.3 | RBC stretching configuration (S1)

2.3.1 | Assumption of an axisymmetric extensional flow in the upstream part

From the simulation performed in the whole domain (S0), three streamlines passing at different distances from the aperture edges are extracted. More precisely, the selected streamlines are chosen such as they pass through points located in the aperture at different distances from the wall: (0,0,0), (0,15,0) and (0,20,0), coordinates given in μm. Respectively denoted by SL1, SL2 and SL3, the streamlines are depicted in Fig. 2. The streamlines curvilinear coordinate system ($\vec{s}, \vec{r}, \vec{q}$) is defined in the following way : $\vec{s}$ is aligned with the streamline; $\vec{q}$ is perpendicular to the streamline and belongs to the plane ($\vec{x}$, $\vec{y}$) and $\vec{r} = \vec{s} \wedge \vec{q}$. Time τ is established from the Lagrangian coordinates system of a fluid particle moving along the selected streamline. Note that time τ = 0 is set in a way that part B and part C (see Fig. 3) refer to negative and positive times, respectively.

The velocity gradients in the curvilinear coordinates system are computed and are shown versus τ in Fig. 5. Regarding the streamline SL1 which crosses the aperture center, Fig. 5A shows that $\dfrac{\partial U_q}{\partial q}$ perfectly equals $\dfrac{\partial U_r}{\partial r}$ for all the upstream part of the aperture. This equality remains valid for the other streamlines SL2 and SL3 except for very small negative values of τ (viz. except very close to the aperture inlet). From those observations, the assumption that a particle moving along a streamline behaves as in an axisymmetric and purely extensional flow up to -12 μs is made.

This assumption is the basis of the S1 simulation type described in the next section.

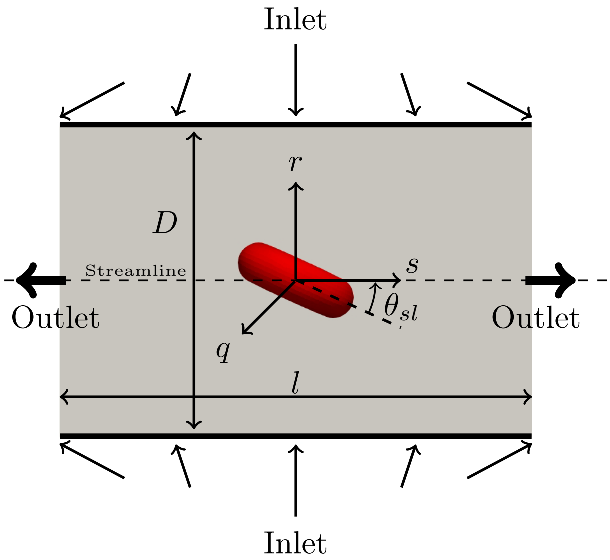

FIGURE 6 Extensional configuration scheme (simulation S1). The particle is initially placed at rest in the center of a cylindrical fluid domain. The cylinder diameter D and length l are respectively equal to 30μm and 50μm. Boundary conditions that insure an extensional velocity field are set according to Eq. 5.

2.3.2 | Extensional configuration setup (S1)

For part B, where the RBC is deformed without impacting the electrical field, a first fluid-structure interaction simulation is performed in a simplified domain used to impose an axisymmetric strain flow. The RBC is supposed to travel in part B along the streamline at the surrounding fluid velocity. The particle is initially placed at the center of a cylindrical fluid domain with possibly a non-zero initial orientation with respect to axis $\vec{s}$, as sketched in Fig. 6. From the time evolution of the stretch rate obtained for a particular streamline (Fig. 5), the following time varying boundary condition is imposed on the lateral boundary ($\mathrm{r}^2 + \mathrm{q}^2 = \frac{D^2}{4}$, s in [-$\frac{l}{2}$,$\frac{l}{2}$]) of the cylinder:

$$\vec{u} = \frac{\partial U_s(t)}{\partial s}\begin{pmatrix} s \\ -\frac{r}{2} \\ -\frac{q}{2} \end{pmatrix} \tag{5}$$

Convective outlet boundary conditions are imposed on the two circular faces s = -l/2 and s = l/2. According to the axisymmetric extensional assumption discussed previously, the particle stretching is performed until 12μs before the aperture entrance.A discussion on the elongation starting point is provided in a following section.

The numerical method employed in YALES2BIO to solve this kind of fluid-structure-interaction problem was detailed in previous publications [22,23,24,25,26]. Briefly, the particle is defined as a drop of fluid enclosed by a membrane. The membrane is supposed to be an infinitely thin and elastic solid that resists to in-plane deformations and out-plane bending loads. The in-plane behavior is modeled according to the Skalak model [30] while the bending resistance is expressed with the Helfrich energy [31]. The Skalak law expresses the strain energy function W_{sk} as a function of the in-plane principal values of strain λ_1 and λ_2:

$$W_{sk} = \frac{G_s}{4}[(\lambda_1^2 + \lambda_2^2 - 2)^2 + 2(\lambda_1^2 + \lambda_2^2 - \lambda_1^2\lambda_2^2 - 1)] + \frac{E_a}{4}(\lambda_1^2\lambda_2^2 - 1)^2 \tag{6}$$

G_s and E_a are material parameters and denote respectively the shear and the area modulus. Discretizing the membrane with triangular elements and making use of the method propounded by Charrier & al. [32], the in-plane elastic forces F_{sk} are computed. As derived by Zhong-can & al. [33], the membrane curvature forces may be written as:

$$\vec{F}_b = E_b[(2\kappa - c_o)(2\kappa^2 - 2\kappa_g + \kappa c_o) + 2\nabla^s\kappa]\vec{n} \tag{7}$$

κ and κ_s represent respectively the mean and the Gaussian curvatures while ∇^s represents the Laplace Beltrami operator and $\vec{n}$ denotes the membrane normal. As for the Skalak model, two material parameters operate in the bending force computation:

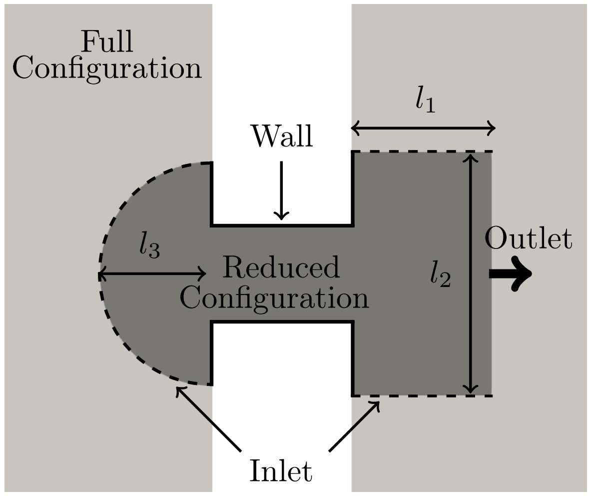

FIGURE 7 Schematic of the axisymmetric reduced configuration for S2. Slice cut of the reduced configuration shown over a small part of the full configuration. On boundaries indicated as Inlet, a velocity profile interpolated from computation S0 is imposed. The domain is characterized by l_1=75μm, l_2=130μm and l_3=60μm.

E_b, the bending modulus and c_o, the spontaneous curvature. More details on the computation of the curvatures may be found in Farutin *et al.*[34].

The fluid-structure interaction is computed thanks to the Immersed Boundary Method (IBM) of Peskin[35]. This method is based on the use of two distinct meshes, one for the fluid and one for the membrane. The grids are not conformal: the Eulerian fluid grid never changes and describes the entire fluid domain (inside and outside the particle). A Lagrangian mesh is used to define the membrane of the RBC. It is a surface mesh defined by triangular elements. The vertices of this mesh (the markers of the membrane) move over time and are generally not at the same location as the fluid nodes. Specific coupling must be performed to make the fluid grid and the membrane grid interact: in the IBM, the membrane forces $\vec{F}_{sk}$ and $\vec{F}_b$ are regularized over the fluid and operate in the velocity advancement through the source term $\vec{f}$ in equation 3. At the end of the time step, the membrane is transported interpolating the fluid velocity on the membrane nodes. Initially developed for regular grids, the use of the IBM on unstructured fluid meshes is enabled by the Reproducing Kernel Particle Method[36]. A variable viscosity field may also be imposed using an indicator function as in the front-tracking method[37]. Detecting the area enclosed by the membrane, the cytosol viscosity denoted ν_{in} may be taken into account. The method and its implementation in the YALES2BIO solver have been used in several publications, showing its ability to recover typical dynamics behaviors of red blood cells in complex flows[17,25,26,38,39].

2.4 | Particle dynamics inside the aperture (S2)

Once stretched during simulation S1, the particle dynamics inside the micro-orifice is solved (simulation S2). The elongated cell is initially placed on the selected streamline at the point corresponding to time -12μs in a reduced configuration of the industrial geometry. The particle orientation θ_{sl} (Fig. 6) at the end of the stretching step is recorded and applied as initial angle of the particle with respect to the streamline for the dynamics simulation. The reduced domain is shown in Fig. 7. The initial velocity field and the boundary conditions on the 'inlet' surfaces (Fig. 7) are interpolated from of the time-converged velocity field obtained in simulation S0. On the wall faces, a zero velocity condition is imposed. On the outlet face a convective outlet boundary condition is imposed to ensure mass conservation. In such a way, a stationary base flow inside the aperture equivalent to the flow simulated in the whole geometry is retrieved.

The numerical method employed for this fluid-structure interaction calculation is identical to the one used for the extensional configuration (S1).

2.5 | Electrical perturbation (S3)

The computation of the electrical perturbation is performed once the particle dynamics simulation inside the micro-orifice is achieved. Interactions between the electrical field and the flow field but also the electrostatic forces acting on the membrane are

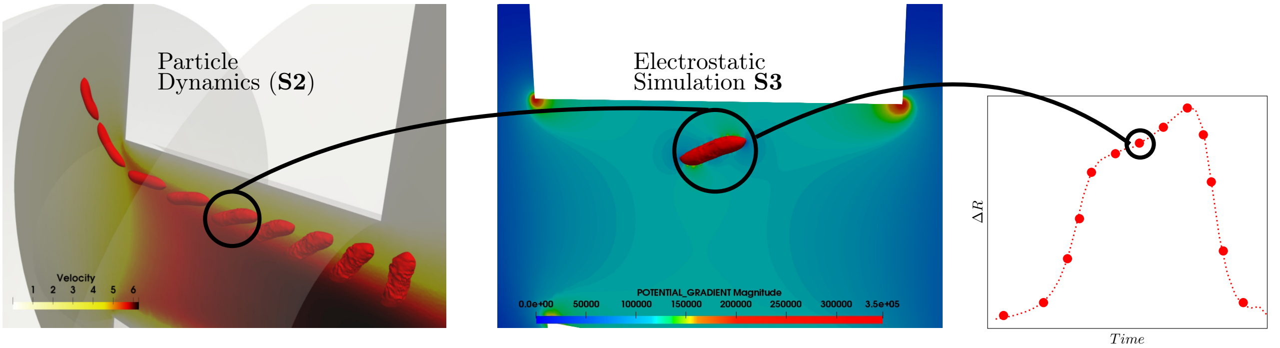

FIGURE 8 Reconstruction of the electrical perturbation from the particle dynamics inside the aperture. The left figure shows typical RBC following positions in the micro-orifice over the velocity field, obtained by numerical simulation. A membrane geometry coming from S2 is used in an electrostatic simulation, see the middle figure. In the middle figure, one of the RBC location is shown over the electrical field, outcome of run S3. From the electrostatic simulation the electrical perturbation ΔR is computed (right figure). Repeating this process for several consecutive membrane positions from S2, the electrical pulse is build point by point.

neglected[7]. In addition, the RBC is viewed as a perfectly isolating particle, as done by Isèbe and Nérin[7]. Those assumptions allow computing the electrical response separately from the dynamical behavior, since the RBC motions depend only on the fluid-structure-interactions. From simulation S2, a series of membrane position is stored (typically every microsecond). For each instant, the membrane shape coming from the dynamics simulation is used to define the position of the cell and the electrostatic Laplace's equation for the electrical potential is solved:

$$\nabla.[\sigma(x)\vec{\nabla}\phi] = 0 \tag{8}$$

As for the dynamics part, our method uses a Lagrangian grid for the membrane and an Eulerian grid for the fluid, over which the Laplace equation is solved. To couple the membrane shape with the electrical field solver, the method used to impose an internal viscosity different from the outside in dynamics simulations is used: the membrane location allows the definition of a variable conductivity coefficient ($\sigma(x)$) different inside and outside the membrane. In order to make the cell isolating, a very small value of conductivity coefficient is imposed inside the cell. This method has been validated on specific test cases[18].

From the electrical potential ϕ, the resistance of the system is deduced and is compared with the resistance of the system without particle: this yields ΔR, the resistance variation caused by the presence of the cell in the electrical field. This calculation is made for several consecutive membrane positions inside the aperture in order to construct the complete electrical perturbation along time, as shown in Fig. 8.

For all the electrostatic computations performed, the conductivity outside the membrane is taken as σ_o=2.27 S.m^{-1} and the conductivity ratio between the inner and outer parts of the RBC equals 10^{-12} to reflect the non-conductive nature of the cell. The electrical potential is set to 13.9V on the cathode and 0.0V on the anode (Fig. 2). The remaining edges of the domain are modeled as non-conducting walls applying a Neumann boundary condition $\vec{\nabla}\phi = \vec{0}$.

Concerning the numerical method employed in YALES2BIO to approximate the electrical potential, Eq 8 is discretized with a second-order method derived from[40]. Once discretized, the linear system is solved with the same DPCG solver as for the Poisson equation in the Navier-Stokes simulations[29].

3 | PIPELINE VALIDATION

The pipeline detailed in the last sections was first tested as explained in this section. From the computation S0, the streamline shown in Fig. 9A (SL2 in Fig. 2) is extracted and different simulations varying the initial conditions are performed. The computed cases are summarized in Fig. 9B. In a first study, which corresponds to cases 1 to 4, the impact of the RBC starting time (or the distance from the aperture at which the cell is deposited, see Fig. 9A) on its dynamics and the resulting impedance pulse is dealt with. For this study, the particle stretching in the extensional configuration (Simulation S1) is bypassed and the RBC is dropped directly on the streamline at different positions, in a full simulation S2. The initial positions are related to times corresponding

(A)

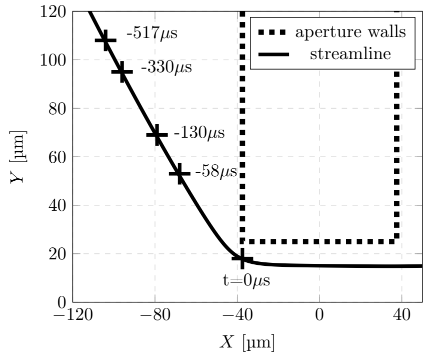

(B)

Case	S1 (μs)	S2 (μs)	Cost (CPU-hour)	$\dot{\epsilon}_0$ (s^{-1})
1	ø	[-517 , 18]	16400	1000
2	ø	[-330 , 18]	12000	2000
3	ø	[-130 , 18]	6500	5000
4	ø	[-58 , 18]	4600	12000
5	[-517 , -12]	[-12 , 18]	2000	1000

FIGURE 9 Summary of the cases performed to assess the effect of the RBC initial position. A: Initial RBC starting positions along the selected streamline.The streamline corresponds to SL2 (Fig. 2) and is extracted from the time converged velocity field of simulation S0. It is selected such as it passes by the point (0, 15, 0). B: Characteristics of the simulations performed in terms of the physical time range in the extensional configuration (S1) and in the reduced configuration (S2). The overall computation cost and the typical strain rate ($\dot{\epsilon}_0$) experienced by the RBC at the beginning of the simulation are also reported.

to the lower bounds reported in the S2 column of Fig. 9B. Then, the capability of the extensional simulation S1 to reproduce the dynamics before the aperture is assessed. More precisely, as introduced in section 2, the RBC is first stretched in an extensional flow simulation S1, then its dynamics inside the orifice is solved in a simulation S2, the final RBC state from S1 being used as an initial condition for S2. This runs sequence corresponds to Case 5 in Fig. 9B and represents exactly the same physical configuration as Case 1. On the contrary, Cases 2-4 denote different initial locations of the RBC. Note however that the final time (τ=18 μs) is the same for all cases.

All cases of Fig 9 B were computed using the same RBC. The shear modulus, the bending modulus, the cytosol viscosity and the spontaneous curvature are imposed as: G_s=2.5× 10^{-6} N.m^{-1}, E_b=6.0 × 10^{-19} N.m, ν_{in}=10.0 m^2.s^{-1}, c_0=0, in agreement with the range of measurements provided in the literature[41,42,26]. Density variations between the internal fluid and the suspending medium are neglected: some test cases to assess the impact of higher density inside the RBCs have shown negligible effect (not shown). The area modulus was set to E_a=2.5× 10^{-1} N.m^{-1} in order to guarantee the membrane area conservation[30]. The membrane encloses a 93 μm^3 volume. The membrane was discretized with triangular elements with a characteristic size of 0.3μm. The initial RBC orientation θ_{sl} with respect to the streamline (Fig. 11) is chosen as 0.43rad for all cases excepted for run 5-S2, where the outcome from run 5-S1 was used. This problem is symmetric with respect to the $(\vec{x}, \vec{y})$ plane, so that the orientation is only defined by an angle in this plane.

The fluid meshes used are presented in Fig. 10. The computation to obtain the carrying flow is performed on the mesh shown in Fig. 10A. The mesh size is imposed to 1.6 μm around the micro-orifice and increases with a growth rate of 1.3 to 500μm. Using the IBM requires a fluid mesh size equal to the membrane mesh size[35,36]. For the extensional configuration, the mesh size is simply imposed to 0.3μm in the whole cylinder (Fig. 10B). In the case of the reduced configuration, the mesh size is refined to 0.3 μm around the streamline, supposed to be a good approximation of the RBC trajectory (Fig. 10C).

For cases 1 to 4, the RBC starting position were willingly placed relatively far from the aperture entrance. A wider reduced configuration is used for those specific cases with l_3=150 μm (Fig. 7). The mesh used for the electrostatic computations is not shown. It was built in the same way than the mesh shown in Fig. 10A, with an additional mesh refinement of 0.3 μm around the part of the streamline inside the sensing zone. In the performed cases, the RBCs follow the streamline within a tolerance margin of 0.3 μm (one mesh size) when traveling in the part upstream of the aperture.

In the following, the Inertia Equivalent Ellipsoid (IEE) of the deforming RBC[43] is used to compare the different cases considered. From the membrane nodes position, the inertia matrix of the RBC at the center of mass is computed and diagonalized

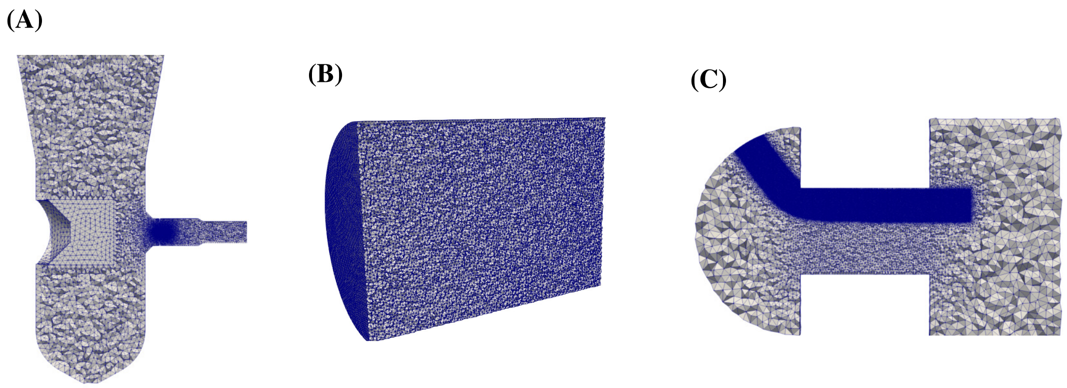

FIGURE 10 Meshes used for the computation of the whole industrial configuration S0 (A), the extensional configuration S1 (B) and the reduced configuration S2 (C). The meshes shown in graphs A, B and C contain approximately 5M, 0.4M and 3M of nodes, respectively.

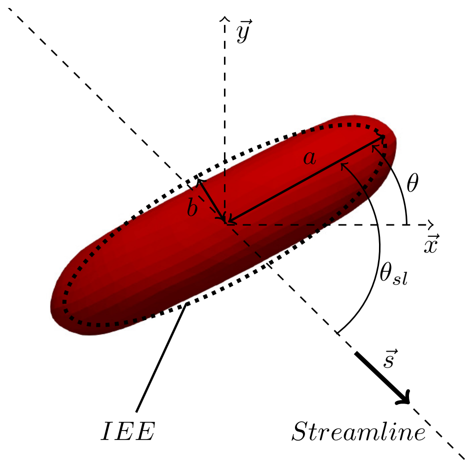

FIGURE 11 Inertia Equivalent Ellipsoid (IEE) parameters and orientation. IEE parameters are shown over a RBC elongated shape. The scheme is represented in the symmetrical plane $(\vec{x}, \vec{y})$ such as $\vec{z}$ is out of plane, as the IEE parameter c.

in order to obtain the eigenvalues and eigenvectors. The IEE parameters, a, b and c are then obtained by solving the following equation:

$$\begin{pmatrix} \lambda_1 & 0 & 0 \\ 0 & \lambda_2 & 0 \\ 0 & 0 & \lambda_3 \end{pmatrix} = \frac{V}{5} \begin{pmatrix} (b^2 + c^2) & 0 & 0 \\ 0 & (a^2 + c^2) & 0 \\ 0 & 0 & (a^2 + b^2) \end{pmatrix} \tag{9}$$

The left and right terms of Eq 9 are respectively the diagonalized RBC inertia matrix and the empirical inertia matrix of an ellipsoid of axes a, b and c, with V denoting the IEE volume. Both are expressed in the eigen-vectors basis. The RBC orientation is defined according to the angle between the IEE axis corresponding to the parameter a and the streamline (θ_{sl}) on the one hand and the $\vec{x}$ axis (θ) on the other hand (Fig. 11).

3.1 | Impact of the starting position on the RBC dynamics

The purpose of this section is to illustrate the dependency of the RBC dynamics with respect to the starting position and to exhibit a starting distance from which the dynamics inside the aperture and the electrical perturbation are converged.

From the IEE orientation (Fig. 12A), one observes that for the upstream part of the micro-orifice ($\tau < 0$), the RBC initial angle progressively decreases to show an orientation perfectly aligned with the streamline just before the aperture entrance. However, inside the micro-orifice, the RBC displays a rotation that depends on the initial starting time. Regarding the ellipsoid parameters in the upstream part, shown in Fig. 12 B-D, the RBC is deformed from an oblate shape to a quasi-prolate shape. Indeed, initially, $a = c$, and both are greater than b. Then, a increases and c decreases whereas b stays almost the same. In the aperture ($\tau > 0$), the RBC is compressed as shown by a decreasing a and an increasing b. This compression occurs as the RBC progressively turns inside the aperture. In fact, for the considered streamline, the RBC crosses region with substantial velocity shears as shown for streamline SL2 in Fig. 2D. The shear stress undergone by the RBC inside the aperture makes it rotate. Besides, the RBC gets compressed when its orientation approaches the compression axis in the shearing region.

The IEE parameters and orientation inside the aperture converge with respect to the RBC starting position. Indeed, taking case 1 as the reference, cases 2, 3 and 4 indicate that taking an earlier starting time (Fig 9 B) gives a result closer to the reference. In addition, case 2 shows superimposed results with case 1, regarding the IEE parameters inside the micro-orifice (Fig. 12). This supports the fact that it is sufficient to use an initial RBC location in the region where the strain rate is of order 2000 s^{-1} in order to accurately describe the RBC dynamics within the aperture.

As a direct consequence of the RBC dynamics, the electrical perturbation also exhibits a dependency with the starting time, as depicted in Fig. 13. As for the IEE parameters, the electrical pulses for cases 1 and 2 are practically identical while cases with a starting point closer to the orifice entry would give inaccurate results. The difference between case 1 and case 4 maxima is evaluated to 10%.

3.2 | Extensional configuration validation

We now compare cases 1 and 5. In both cases, the RBC is depositted at the same location, but in case 5, the dynamics far from the aperture is computed in the dedicated extensional configuration (S1) while it is computed in the full configuration in case 1.

First, Fig. 12 shows that the run 5-S1 is in good agreement with the first part ($\tau <$ - 12 μs) of Case 1. Thus the extensional axi-symmetrical configuration S1 is proven to be suitable to reproduce the early stage of the RBC deformation. It should be noted that the orientation corresponding to run 5-S1 in Fig. 12D is evaluated as the orientation of the IEE a-axis with respect to axis $\vec{s}$ of the extensional configuration (Fig. 6). Then, comparing run 5-S2 to case 1, one may observe that a RBC dropped in the reduced configuration after being stretched in an extensional configuration behaves as if it had undergone the full elongation before entering in the aperture. Moreover, cases 1 and 5 are perfectly consistent in terms of impedance pulse, as shown in Fig. 13. The approach of solving separately the particle elongation occurring in part B allows a computation cost reduced by a factor 8 (cases 1 and 5 Fig. 9B). Regarding the results shown in Fig. 12 and Fig. 13, simulations should start at least 330 μs before the orifice entrance. Due to the low computation cost of the extensional simulation, the choice was made to simulate the cell elongation in the configuration S1 from -517 μs to -12 μs. Computation S2 then starts from -12 μs and ends after the RBC leaves the micro-orifice.

4 | APPLICATIONS

A diversity of electrical pulse signatures is reported in the literature. Grover[5] obtained "bell-shaped" and "M-shapped" pulses when using rigid spheres. As it was shown later, for the case of spheres, the pulses shapes depict the electrical field squared along the particle trajectories[8] (see Eq. 2). Considering rigid ellipsoid[44], fixed RBC[45] or normal RBC[44], many complex signatures are found in addition to the "bell-shaped" and "M-shapped" pulses. Enforcing the particle path, Kachel[45] found that those complex pulses shapes are retrieved for near wall trajectories while "bell-shaped" pulses are obtained for centred paths. Near the aperture edges, velocity shear causing changes in the shape factor and electrical field inhomogeneities are present. Those edge-effects are still misunderstood and known to skew the volume measurement of the particles[46].

The aim of this section is to illustrate how the numerical pipeline of Section 2 can be used to understand the edge-effects. In a first part, the numerical results are used for explaining typical pulses signatures obtained with an experimental approach. Then, a method to derive the RBC shape factor as a post-processing outcome of a numerical simulation is presented. It is then shown that the computed shape factor evolution and the electrical field observed by a particle can be combined to provide a good approximation of the pulse signature.

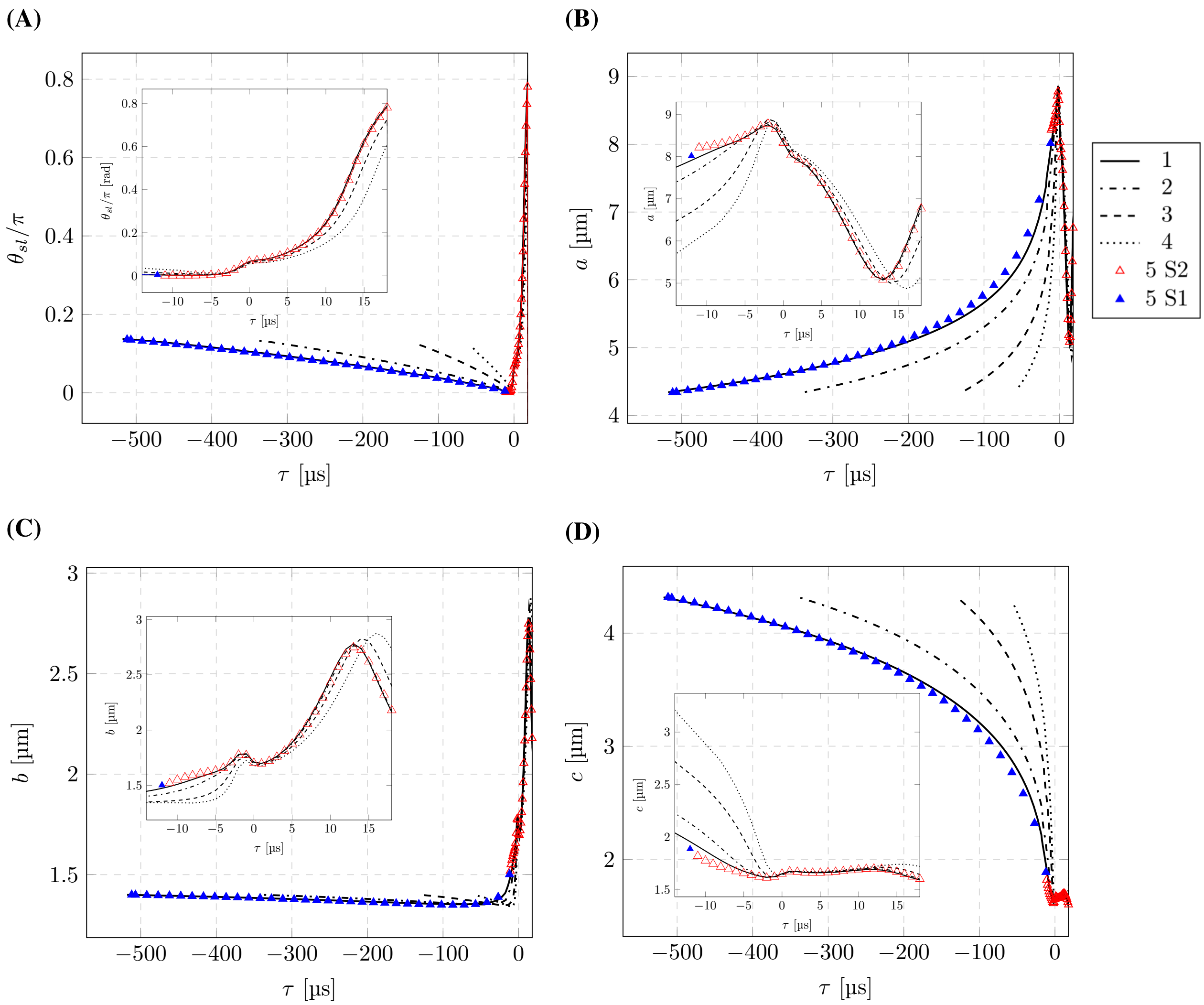

FIGURE 12 Inertia equivalent ellipsoid principal axis and orientation for cases summarized in Fig. 9B. A: Orientation of IEE axis a with the trajectory as defined in Fig. 11. B: IEE parameter a, that tends to align with the extensional direction. C: IEE parameter b, perpendicular to a in the symmetrical plane $(\vec{x},\vec{y})$. D: IEE parameter c that is out of the symmetrical plane lined up with $\vec{z}$.

4.1 | Pulses analysis

Considering a centred and a near-wall path, the so-called "edge-effects" are first pointed out. Both rigid beads and RBC were considered in this study. On the one side, dealing with rigid spheres emphasises the electrical field inhomogeneity effects, because the shape factor of the particle is obviously constant in this case. On the other side, dealing with RBCs which are highly deformable highlights impact of the particle dynamics on the electrical perturbation.

The two streamlines investigated contain the geometrical points (0,0,0) and (0,20 μm,0), corresponding to SL1 and SL3 of Fig. 2, respectively. Using the method of Section 2, the RBC dynamics and the induced electrical perturbation are simulated for those two streamlines. The RBC parameters are set as in section 3 except for the internal viscosity which is 18×10^{-6} m^2.s^{-1}, to take into account the room temperature of the experimental acquisition[47]. When considering a rigid and spherical particle, there is no need for a preliminary stretching simulation, since no deformation nor rotation are expected. That is why, for the rigid beads, computations start by depositing the sphere 5μs before the aperture entrance in the reduced configuration. Rigid spheres were modeled as spherical cells of diameter 5 μm. Beside, G_s and ν_{in} were set to 2.5×10^{-3} N.m^{-1} and 50×10^{-6} m^2.s^{-1}, in order

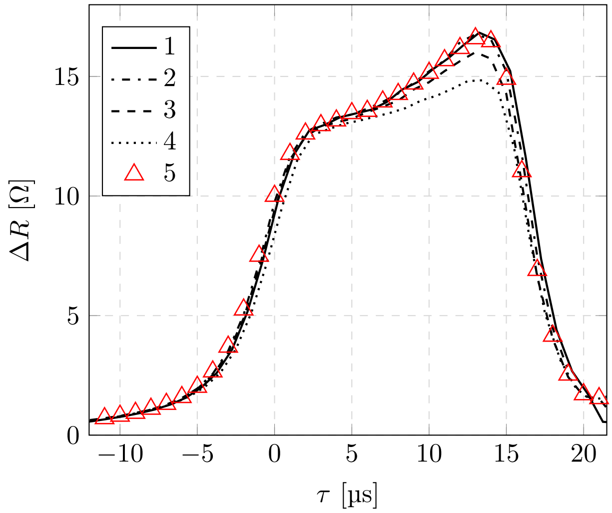

FIGURE 13 Impedance pulses obtained from a RBC with the different initial conditions that are summarized in Fig. 9B.

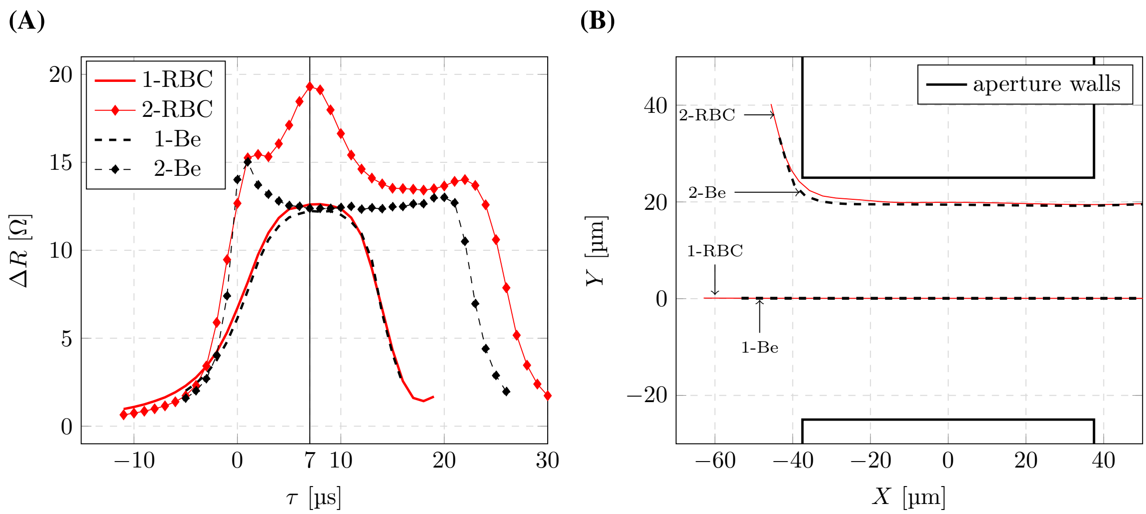

FIGURE 14 Impedance pulses obtained numerically for rigid beads and RBC considering two different streamlines. The considered streamlines are SL1 and SL3 illustrated in Fig. 2, that pass by points (0,0,0) and (0,20μm,0), respectively. Graph A shows the resistance perturbation versus time while graph B depicts the corresponding trajectories. The vertical continuous line highlights the moment at which occurs the peak, characteristic of a pulse generated by a RBC pursuing a near wall trajectory (2-RBC).

to ensure that the particle remains spherical during the simulation (variations in diameter were less than 1 %). The remaining particle parameters were taken as in Section 3.

Experimental acquisitions were performed thanks to a ABX Micros 60 system from HORIBA Medical. A needle withdraws a few μL from a blood sample tube. The blood is then transferred to the counting tank and diluted by a factor 1/15000 in the Minidil electrolytic reagent (HORIBA Medical). Finally, the dilution is pumped through the micro-orifice and the signal recording is started. The counting tank is the same as the one depicted in Fig. 2. The pressure drop imposed to produce the flow through the aperture and the electrical potential imposed to the electrodes conform to the boundary conditions imposed in the simulations (section 2.2 and 2.5). The tension pulses are treated and amplified by the ABX Micros 60 system. The electrical signal after the amplifier is given as an input of an in-house LabVIEW code that registers the electrical perturbations. Two series of acquisitions were achieved, one for a latex beads sample (5 μm of diameter) and one for a sample of blood coming from a healthy patient within 4 hours after extraction.

4.1.1 | Numerical Results

The electrical responses obtained numerically are shown in Fig. 14A, while the trajectories followed by the particles are depicted in Fig. 14B. The rigid bead and RBC cases are denoted by Be and RBC respectively while the centered and off-centered streamlines are numbered with 1 and 2. For the centered path, "bell-shaped" pulses with a short duration are obtained for both RBC and rigid sphere cases (Fig. 14A, cases 1-Be and 1-RBC). However, when considering the case of a trajectory near the aperture edges (2-Be and 2-RBC), the pulse duration increases owing to low velocities. For the sphere case 2-Be, a shorter pulse is obtained compared to 2-RBC. Looking at trajectories 2-RBC and 2-Be (Fig. 14B), it is observed that the sphere is slightly deflected towards the aperture axis when entering the aperture, thus decreasing the pulse duration. Note that during simulation S2, particles trajectories are free to deviate from the streamline. Remind that the latter is only needed to assess the particle initial state and position for computation S2. However, for the cases considered in this study, deviations between streamlines and trajectories remain small.

Figure 15 shows the IEE parameters and orientation θ (see Fig. 11) for cases 1-RBC and 2-RBC. For the centered path, the RBC stays aligned with the orifice principal axis (Fig. 15A) and shows a stable shape inside the aperture (Fig. 15B, 15C and 15D for τ>0). As it will be discussed in a following section, the RBC shape factor is almost constant in the case of a centered trajectory, thus explaining the similarity between cases 1-Be and 1-RBC (Fig. 14). In contrast, the RBC following the near-wall trajectory undergoes a rotation , as the evolution of the θ angle shows (Fig. 15A). Moreover, as for the test case of section 3, the initial prolate ellipsoid shape is compressed as the RBC rotates (Fig. 12). It is interesting to note that the moment at which a peak occurs in the electrical response corresponds to the moment at which the RBC is perpendicular to the orifice principal axis (Fig. 14A and Fig. 15A at approximately 7 μs). As illustrated by Golibersuch[11], the RBC rotation induces an increasing of the shape factor and a peak on the electrical perturbation is observable. In their study, Golibersuch used a long aperture (about 420 μm of length) allowing each particle to rotate several times. In industrial Coulter counters, short apertures are generally employed and the Poiseuille velocity profile is not reached. At the center of the micro-orifice, a flat velocity profile is obtained, and rotation may occur only for near wall trajectories, where velocity shear is present.

Particles following a near wall trajectory pass through dense electrical field regions when crossing the inlet and outlet sections of the micro-orifice (Fig 2 C). Those regions explain the typical "M-shaped" pulse obtained for the sphere case 2-Be. Concerning RBC (2-RBC), the peak comes in addition to the M-shape.

It should be noted that despite the difference between the particles volume (93 μm^3 for the RBC and 65 μm^3 for the sphere), the pulses 1-Be and 1-RBC have almost the same amplitude. This is explained by a substantial difference in shape factor between spheres and an elongated object as RBCs pursuing central trajectories[8]. Indeed, for the case of spheres, a shape factor of 1.5 was evaluated by many autors[5,9], while for an elongated object a shape factor around 1.0 is expected[46].

4.1.2 | Comparison with experimental data

In this part, numerical results of the previous section are compared with experimental data. More precisely, pulses 1-Be and 2-Be are compared with pulses obtained from a latex bead sample while cases 1-RBC and 2-RBC are compared with electrical perturbations obtained when analyzing a blood sample. Stating that the pulse duration gives directly an information on the pursued trajectory, the choice was made to compare the shortest and longest experimental pulses with simulated pulses generated from the centered and near-wall paths, respectively. The pulse duration are computed as in[48].

Converting the measured tension pulses to resistive pulses is not straightforward because of the signal treatements performed by the Micros 60 hardware system. Therefore, experimental and numerical data are scaled in amplitude before comparisons. For a given experimental acquisition, the pulses are scaled with the mean of the "bell-shaped" pulses maximum. Those latter are extracted from the entire acquisition by the use of a convenient pulse duration threshold. Numerical pulses generated from the rigid sphere and the RBC are scaled with the maximum of pulses 1-Be and 1-RBC, respectively (Fig. 14).

Once the data scaled, the numerical pulses durations are computed and used for extracting from the experimental acquisition signatures having the same duration, with a tolerance margin of 1 μs. Figure 16 displays the numerical results superimposed with experimental pulses having the same length. The predicted numerical results are retrieved in the experiment. For both latex bead and RBC cases (Fig. 16A and 16C), the shortest experimental pulses display a bell-shape. The typical M-shaped pulses are

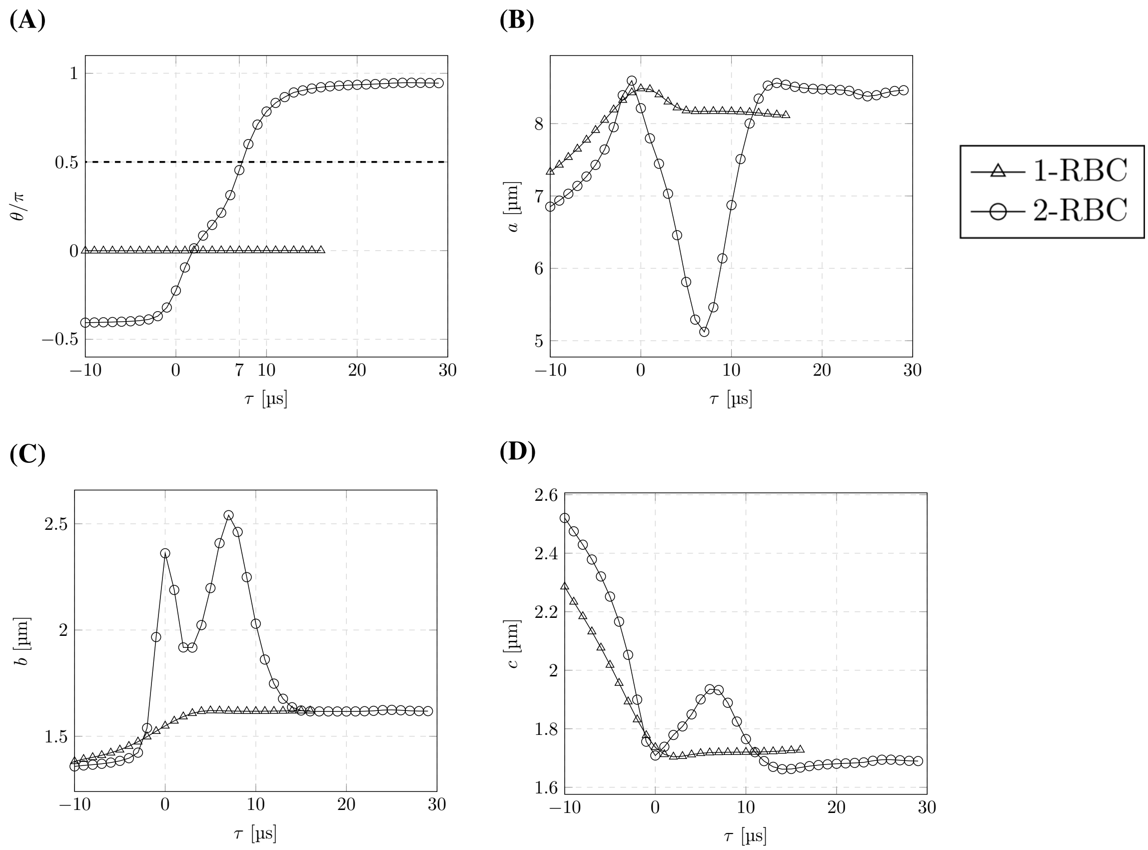

FIGURE 15 RBC IEE orientation and parameters for cases 1-RBC and 2-RBC of Fig 14.

observed by extracting the longest pulses induced by spherical particles (Fig. 16B) . The peak characteristic of the RBC rotation is also observable experimentally for the case of the longest pulses generated by RBCs (Fig. 16D).

4.2 | Theoretical modeling of the electrical perturbations

By comparing the experiment with the simulation results, a part of the experimental pulses was explained in terms of the particle rotation and electrical field inhomogeneities . Hereafter, the shape factor variations are modeled. The aim of this modeling effort is to provide a finer analysis of the pulses signatures and uncorrelate the dynamical effects from the electrical ones.

In the case of rigid spheres, the shape factor f_s is constant, so that, a linear relation between the squared electrical field and the electrical perturbation ΔR is expected, see Eq. 2. From an electrostatic simulation performed without particles, the electrical field E is interpolated along the trajectories of Fig. 14. Figure 17 shows the scaled squared electrical field along the particle trajectory and the scaled pulses according axis $\vec{x}$ for cases 1-Be and 2-Be. A good agreement of E^2 with the electrical perturbation is found. This result fully supports Kachel's statement[8] that, under the assumption of a constant shape factor, ΔR is directly proportional to E^2.

When considering deformable particles such as RBC, deformations and rotation may cause shape factor variations, in particular for near wall trajectories. In such a way, there is no linearity between E^2 and ΔR (Eq. 2). In the following, the RBC shape factor is modeled using IEE orientation and parameters. Provided one of the ellipsoid principal axis is aligned with the electrical field $\vec{E}$, Velick and Gorin[9] states that, in the case of a non-conducting ellipsoid immersed in a homogeneous electrical field, the shape factor may be written as:

$$f_s = \frac{2}{2 - a.b.c.L_\alpha} \tag{10}$$

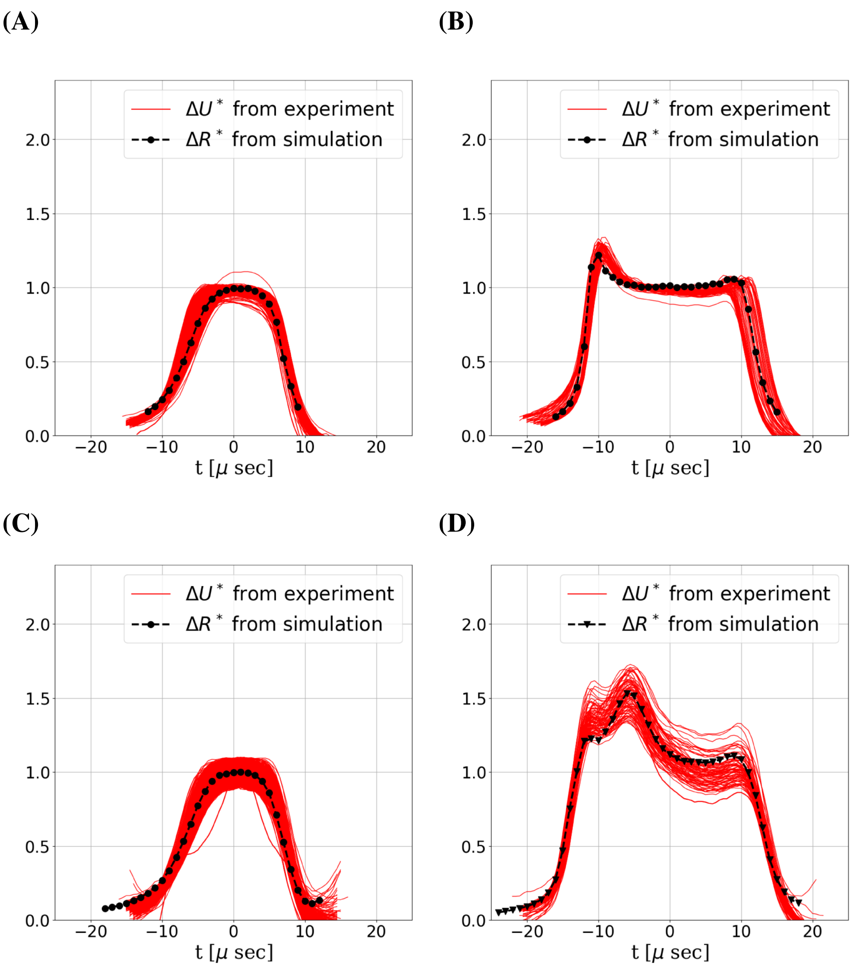

FIGURE 16 Numerical pulses of Fig. 14 superimposed with relevant experimental data. Graphs A and B compare cases 1-Be and 2-Be with shortest and longest experimental pulses obtained from a latex bead sample, respectively. In a same way, graphs C and D compare 1-RBC and 2-RBC with the shortest and longest pulses obtained form a blood sample. Experimental pulses are measured as tension changes, ΔU while numerical pulses are computed as a resistance variation ΔR, that is why the amplitudes are scaled with the "bell shaped" pulses maximum.

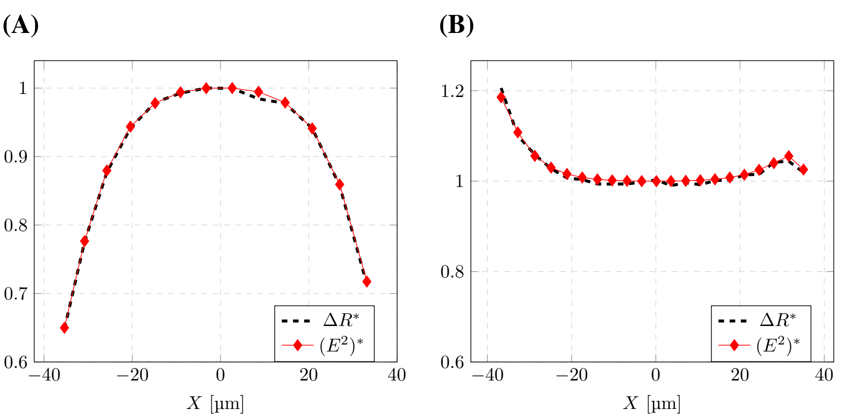

FIGURE 17 Comparison between the resistive perturbation obtained from a rigid bead and the squared electrical field along the particle trajectory. A and B are relative to cases 1-Be and 2-Be respectively. In the shown graphs, each quantity $\phi(X)$ is scaled as : $\phi^*(X) = \phi(X)/\phi(X=0)$, with $\phi \in [\Delta R, E^2]$.

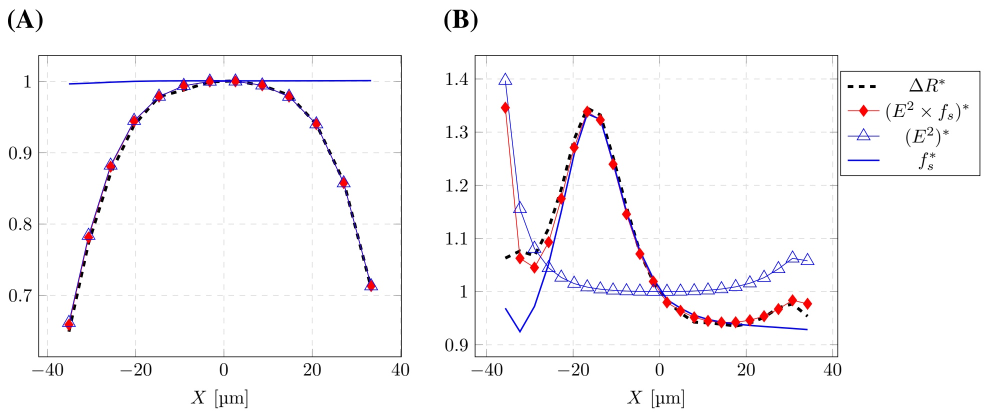

FIGURE 18 Modeling of the pulse signatures for the case of a deformable particle such as RBC. On those graphs, the pulse, the squared electrical field, the shape factor and the product of the squared electrical field with the shape factor are shown. A and B refer to cases 1-RBC and 2-RBC of Fig. 14. In the shown graphs, each quantity $\phi(X)$ is scaled as : $\phi^*(X) = \phi(X)/\phi(X = 0)$, with $\phi \in [\Delta R, E^2, E^2 \times f_s, f_s]$.

where a, b and c denote the ellipsoid parameters and L_α is an elliptical integral that depends on the ellipsoid axis that is lined up with $\vec{E}$. As an example, if axis a is aligned with the electrical field, one has:

$$L_\alpha = L_a = \int_0^\infty \frac{d\lambda}{(a^2+\lambda)^{3/2}(b^2+\lambda)^{1/2}(c^2+\lambda)^{1/2}} \tag{11}$$

For the computation of L_b and L_c, the ellipsoid parameters a, b and c are simply interchanged in Eq. 11. In order to take into account the RBC orientation inside the aperture, Eq. 10 is combined with the following relation [10]:

$$f_s = f_{//} - cos^2[\theta(f_{//} - f_\perp)] \tag{12}$$

where θ is the orientation of the IEE a-axis with respect to the electrical field, while the terms $f_{//}$ and $f_\perp$ denote the shape factor of the particle when the a-axis is aligned and perpendicular to the electrical field. Those latter are computed with the use of Eq.10 using respectively L_a and L_b.

From the RBC IEE parameters reported in Fig. 15, the shape factor evolution inside the aperture is computed for Cases 1-RBC and 2-RBC by the use of Eq. 12. Figure 18 shows the scaled shape factor, the scaled electrical field squared, the scaled pulse and the scaled product of the shape factor with the electrical field squared. For the case of a centered path (Fig. 18A), the shape factor is constant within the micro-orifice as it was suggested observing the constant IEE parameters and orientation in Fig. 15. In agreement with Eq. 2, the scaled electrical perturbation is then superimposed with the squared electrical field. For a near wall trajectory, the RBC rotation and deformation make the shape factor vary during the particle evolution inside the orifice. The squared electrical field is no more sufficient to explain the pulse signature, however, as provided by equation 2, the product of f_s with E^2, shows a good comparison with the electrical perturbation. A loss of accuracy is nevertheless observed when approaching the aperture limits (x=$\pm$ 37.5μm). On the orifice limits, the electrical field $\vec{E}$ is not aligned with axis $\vec{x}$, thus the IEE orientation θ does not measure the expected angle for equation 12, thus explaining the differences. A correction would need to be implemented to make the model relevant outside the orifice.

5 | CONCLUSION

Coulter counters generally used in the industry involve a tank separated in two parts by a micro-orifice. The detection zone that is almost restricted to the micro-orifice is included in a bigger area where particles undergo deformations. The time required for a particle to cross the aperture is smaller by several orders of magnitude than the time spent by the particle in the whole deformation area. For this reason, simulating the particle behavior in the entire deformation area is not practicable because of the required computational cost.

A numerical pipeline allowing the simulation of deformable particles in a Coulter counter is proposed. Upstream of the aperture, a purely axisymmetric flow is evidenced in the geometry of interest, so that the simulation of the particle deformation that occurs upstream of the aperture is well predicted thanks to an extensional configuration that requires a small computationnal domain only. The particle dynamics inside the orifice is then solved taking the elongated particle as initial state. Finally, the resistive perturbation induced by the particle evolution inside the aperture is obtained from a series of electrostatic simulations assuming that the particle is perfectly isolating.

As illustration cases, RBC and rigid spheres were considered. However, the method can be extended to other types of deformable or rigid particles. The numerical pulses generated for rigid spheres and deformable RBCs show very good qualitative comparisons with experimental data . Dealing with centered and off-centered trajectories, the electrical and dynamical edge-effects are pointed out. Regions with a dense electrical field near the aperture walls lead to "M-shapped" pulses for spherical particles. RBCs crossing the orifice along the walls rotate and induce a peak on the electrical perturbation that comes in addition to the electrical effect.

Using the inertia equivalent ellipsoid and shape factor analytical models provided in the literature, the evolution of the shape factor during the particle evolution inside the aperture is provided. As stipulated by the empirical Eq. 2, linearity between the electrical perturbation and the product of the shape factor with the squared electrical field is retrieved. Considering rigid spheres, for which the shape factor remains constant, the squared electrical field is directly proportional to the resistance variation. The use of the numerical simulation with the shape factor modeling allows a better understanding on the electrical and dynamical respective contributions on the edge-effects. The analysis presented also provides a useful tool to assess the particle deformability impact on the electrical perturbation.

The presented works and results were dedicated to the Micros 60 (HORIBA Medical) operating system. The propounded pipeline remains applicable for other configurations, provided the assumption of an axisymmetric extensional flow in the upstream part of the aperture can be made. It should be noted that the required elongation time should be established before applying the propounded pipeline for other configurations. Finally, note that in the range of the electrical field observed in the studied configuration (in the order of 1.0×10^{6} V.m^{-1}), RBC electro-deformations were reported[49 50], so that greater deformation should be expected if dielectrophoretic (DEP) forces were taken into account. The membrane viscosity was not accounted for neither, despite the short loading times (about a few 10 μm) experienced by the RBC in this kind of configuration. Further investigations about the impact of these effects are intended to in the future. Still, good comparison with experimental data was obtained, demonstrated that the proposed pipeline and current assumptions are appropriate to represent the main mechanisms at play.

ACKNOWLEDGEMENTS

We thank Dr Moureau, Dr Lartigue (CORIA, UMR 6614) and the SUCCESS scientific group for providing the YALES2 code, which served as a basis for the development of YALES2BIO. Simulations with YALES2BIO were performed using HPC resources from GENCI-CINES (Grants No. 2017-A0020307194 and A0040307194) and from the platform MESO@LR

References

1. Constantino BT. The Red Cell Histogram and The Dimorphic Red Cell Population. *Laboratory Medicine* 2011; 42(5): 300-308. doi: 10.1309/LMF1UY85HEKBMIWO

2. Gardner FH, Bessman JD, Gilmer J. Improved Classification of Anemias by MCV and RDW. *American Journal of Clinical Pathology* 1983; 80(3): 322-326. doi: 10.1093/ajcp/80.3.322

3. Yeşil A, Senateş E, Bayoğlu IV, Erdem ED, Demirtunç R, Kurdaş Övünç AO. Red cell distribution width: a novel marker of activity in inflammatory bowel disease. *Gut and Liver* 2011; 5(22195244): 460–467.

4. Coulter WH. Means for counting particles suspended in a fluid.US Patent 2,656,508. 1953.

5. Grover NB, Naaman J, Ben-Sasson S, Doljanski F. Electrical Sizing of Particles in Suspensions: I. Theory. *Biophysical Journal* 1969; 9: 1398-1414.

6. Hurley J. Sizing Particles with a Coulter Counter. *Biophysical Journal* 1970; 10: 74–79.

7. Isèbe D, Nérin P. Numerical simulation of particle dynamics in an orifice-electrode system. Application to counting and sizing by impedance measurement. *International Journal for Numerical Methods in Biomedical Engineering* 2013; 29(4): 462–475.

8. Kachel V. Sizing of Cells by the Electrical Resistance Pulse Technique: Methodology and Application in Cytometric Systems. *Cell Analysis* 1982; 1: 195–331.

9. Velick S, Gorin M. The Electrical Conductance of Suspensions of Ellipsoids and its Relation to the Study of Avian Erythrocytes. *Journal of General Physiology* 1940; 23(6): 753–71.

10. Breitmeyer MO, Lightfoot EN, Dennis WH. Model of red blood cell rotation in the flow toward a cell sizing orifice. *European Biophysics Journal* 1971; 11: 146–157.

11. Golibersuch D. Observation of Aspherical Particle Rotation in Poiseuille Flow via the Resistance Pulse Technique: I. Application to Human Erythrocytes. *Biophysical Journal* 1973; 13(3): 265 - 280.

12. Fedosov DA, Pan W, Caswell B, Gompper G, Karniadakis GE. Predicting human blood viscosity in silico. *Proceedings of the National Academy of Sciences USA* 2011; 108(29): 11772–11777.

13. Freund JB. Numerical Simulation of Flowing Blood Cells. *Annual Review of Fluid Mechanics* 2014; 46: 67–95.

14. Matsunaga A, Imai Y, Wagner C, Ishikawa T. Reorientation of a single red blood cell during sedimentation. *Journal of Fluid Mechanics* 2016; 806: 102–128.

15. Balogh P, Bagchi P. A computational approach to modeling cellular-scale blood flow in complex geometry. *Journal of Computational Physics* 2017; 334: 280 - 307. doi: https://doi.org/10.1016/j.jcp.2017.01.007

16. Guo J, Pui TS, Rahman ARA, Kang Y. 3D numerical simulation of a Coulter counter array with analysis of electrokinetic forces. *Electrophoresis* 2013; 34(3): 417–424.

17. Lanotte L, Mauer J, Mendez S, et al. Red cells' dynamic morphologies govern blood shear thinning under microcirculatory flow conditions. *Proceedings of the National Academy of Sciences USA* 2016; 113(47): 13289–13294.

18. Gibaud E. *Numerical simulation of red blood cells flowing in a blood analyzer*. PhD thesis. Université de Montpellier, 2015.

19. Zmijanovic V, Mendez S, Moureau V, Nicoud F. About the Numerical Robustness of Biomedical Benchmark Cases: Interlaboratory FDA's Idealized Medical Device. *International Journal for Numerical Methods in Biomedical Engineering* 2017; 33(1): e02789:1–17.

20. Méndez Rojano R, Mendez S, Nicoud F. Introducing the pro-coagulant contact system in the numerical assessment of device-related thrombosis. *Biomechanics and Modeling in Mechanobiology* 2018; 17(3): 815-826.

21. Puiseux T, Sewonu A, Meyrignac O, et al. Reconciling PC-MRI and CFD: an in-vitro study. *accepted in NMR in Biomedicine* 2019.

22. Mendez S, Gibaud E, Nicoud F. An unstructured solver for simulations of deformable particles in flows at arbitrary Reynolds numbers. *Journal of Computational Physics* 2014; 256(1): 465–483.

23. Sigüenza J, Mendez S, Ambard D, et al. Validation of an immersed thick boundary method for simulating fluid-structure interactions of deformable membranes. *Journal of Computational Physics* 2016; 322: 723–746.

24. Sigüenza J, Mendez S, Nicoud F. How should the optical tweezers experiment be used to characterize the red blood cell membrane mechanics?. *Biomechanics and Modeling in Mechanobiology* 2017; 16: 1645-1657.

25. Mendez S, Abkarian M. In-plane elasticity controls the full dynamics of red blood cells in shear flow. *Physical Review Fluids* 2018; 3(101101(R)).

26. Mauer J, Mendez S, Lanotte L, et al. Flow-Induced Transitions of Red Blood Cell Shapes under Shear. *Physical Review Letters* 2018; 121(118103).

27. Moureau V, Domingo P, Vervisch L. Design of a massively parallel CFD code for complex geometries. *Comptes Rendus Mécanique* 2011; 339(2-3): 141–148.

28. Kim J, Moin P. Application of a Fractional-Step Method to Incompressible Navier-Stokes Equations. *Journal of Computational Physics* 1985; 59: 308–323.

29. Malandain M, Maheu N, Moureau V. Optimization of the deflated Conjugate Gradient algorithm for the solving of elliptic equations on massively parallel machines. *Journal of Computational Physics* 2013; 238: 32–47.

30. Skalak R, Tozeren A, Zarda RP, Chien S. Strain energy function of red blood cell membranes. *Biophysical Journal* 1973; 13: 245–264.

31. Helfrich W. Elastic Properties of Lipid Bilayers: Theory and Possible Experiments. *Z. Naturforsch* 1973; 28 c: 693–703.

32. Charrier JM, Shrivastava S, Wu R. Free and constrained inflation of elastic membranes in relation to thermoforming non-axisymmetric problems. *The Journal of Strain Analysis for Engineering Design* 1989; 24(2): 55–74.

33. Zhong-can OY, Helfrich W. Bending energy of vesicle membranes: General expressions for the first, second, and third variation of the shape energy and applications to spheres and cylinders. *Physical Review A* 1989; 39(10): 5280–5288.

34. Farutin A, Biben T, Misbah C. 3D numerical simulations of vesicle and inextensible capsule dynamics. *Journal of Computational Physics* 2014; 275: 539–568.

35. Peskin CS. The immersed boundary method. *Acta Numerica* 2002; 11: 479–517.

36. Pinelli A, Naqavi IZ, Piomelli U, Favier J. Immersed-boundary methods for general finite-difference and finite-volume Navier–Stokes solvers. *Journal of Computational Physics* 2010; 229: 9073–9091.

37. Unverdi SO, Tryggvason G. A Front-Tracking Method for Viscous, Incompressible, Multi-fluid Flows. *Journal of Computational Physics* 1992; 100: 25–37.

38. Loiseau E, Massiera G, Mendez S, Aguilar Martinez P, Abkarian M. Microfluidic Study of Enhanced Deposition of Sickle Cells at Acute Corners. *Biophysical Journal* 2015; 108: 2623-2632.

39. Iss C, Midou D, Moreau A, et al. Self-organization of red blood cell suspensions under confined 2D flows. *Soft Matter* 2019; 15: 2971-2980.

40. Specogna R, Trevisan F. A discrete geometric approach to solving time independent Schrödinger equation. *Journal of Computational Physics* 2011; 230: 1370–1381.

41. Cordasco D, Yazdani , Bagchi P. Comparison of erythrocyte dynamics in shear flow under different stress-free configurations. *Physics of Fluids* 2014; 26(041902). doi: 10.1063/1.4871300

42. Abkarian M, Viallat A. Fluid-Structure Interactions in Low-Reynolds-Number Flows. *On the importance of red blood cells deformability in blood flow. Royal Society of Chemistry, London* 2016: 347-462.

43. Ramanujan S, Pozrikidis C. Deformation of liquid capsules enclosed by elastic membranes in simple shear flow: large deformations and the effect of fluid viscosities. *Journal of Fluid Mechanics* 1998; 361: 117–143.

44. Grover NB, Naaman J, Ben-Sasson S, Doljanski F. Electrical Sizing of Particles in Suspensions: III. Rigid Spheroids and Red Blood Cells. *Biophysical Journal* 1972; 12: 1099-1116.

45. Kachel V. Electrical Resistance Pulse Sizing: Coulter sizing. In: No. 4. Wiley-Liss, Inc.; 1990: 45-80.

46. Waterman CS, Atkinson EEJ, Wilkins BJ, Fischer CL, Kimzey SL. Improved Measurement of Erythrocyte Volume Distribution by Aperture-Counter Signal Analysis. *Clinical Chemistry* 1975; 21(9): 1201-1211.

47. Kelemen C, Chien S, Artmann GM. Temperature Transition of Human Hemoglobin at Body Temperature: Effects of Calcium. *Biophysical Journal* 2001; 80: 2622-2630.

48. Zheng Y, Shojaei-Baghini E, Azad A, Wang C, Sun Y. High-throughput biophysical measurement of human red blood cells. *Lab on a Chip* 2012; 12(14): 2560–2567.

49. Qiang Y, Liu J, Du E. Dielectrophoresis Testing of Nonlinear Viscoelastic Behaviors of Human Red Blood Cells. *Micromachines* 2018; 9(1). doi: 10.3390/mi9010021

50. Nodargi NA, Bisegna P, Caselli F. Effective computational modeling of erythrocyte electro-deformation. *Meccanica* 2017; 52(3): 613–631. doi: 10.1007/s11012-016-0424-0